natureresearch

https://doi.org/10.1038/s41567-020-01156-1

Supplementary information

Polarization entanglement-enabled quantum holography

In the format provided by the authors and unedited

Supplementary information: Polarisation entanglement-enabled quantum holography

Hugo Defienne[1], Bienvenu Ndagano[1], Ashley Lyons[1] & Daniele Faccio[1]

[1] *School of Physics and Astronomy, University of Glasgow, Glasgow G12 8QQ, UK*

1 Details on intensity correlation measurement

This section provides more details about the intensity correlation measurement performed by the EMCCD camera. Further theoretical details can be found in [1].

An EMCCD camera can be used to reconstruct the spatial (a) intensity distribution $I(\mathbf{k})$ and (b) intensity correlation distribution $\Gamma(\mathbf{k_1}, \mathbf{k_2})$ of photon pairs, where $\mathbf{k}$, $\mathbf{k_1}$ and $\mathbf{k_2}$ correspond to positions of camera pixels. To do that, the camera first acquires a set of N frames $\{I_l\}_{l \in [\![1,N]\!]}$ using a fixed exposure time. Then:

(a) The intensity distribution is reconstructed by averaging over all the frames:

$$I(\mathbf{k}) = \frac{1}{N} \sum_{l=1}^{N} I_l(\mathbf{k}) \tag{1}$$

(b) The intensity correlation distribution is reconstructed by performing the following substation:

$$\Gamma(\mathbf{k_1}, \mathbf{k_2}) = \frac{1}{N} \sum_{l=1}^{N} I_l(\mathbf{k_1}) I_l(\mathbf{k_2}) - \frac{1}{N-1} \sum_{l=1}^{N-1} I_l(\mathbf{k_1}) I_{l+1}(\mathbf{k_2}) \tag{2}$$

> Under illumination by the photon pairs, intensity correlations in the left term of the subtraction originate from detections of both real coincidences (two photons from the same entangled pair) and accidental coincidences (two photons from two different entangled pairs), while intensity correlations in the second term originate only from photons from different entangled pairs (accidental coincidence) because there is zero probability for two photons from the same entangled pair to be detected in two succesive images. A subtraction between these two terms leaves only genuine coincidences, that are proportional to the spatial joint probability distribution of the pairs.

In our work, we use this technique for measuring correlation between pairs of symmetric pixels $\mathbf{k}$ and $-\mathbf{k}$ to reconstruct intensity correlation images $R(\mathbf{k})$. These images correspond exactly to the anti-diagonal component of the complete intensity correlation distribution $R(\mathbf{k}) = \Gamma(\mathbf{k}, -\mathbf{k})$. Fig. A illustrates these different types of measurements in the case of the experiment described in Fig.1 of the manuscript when Bob displays a phase shift $+\pi$ on his SLM. Fig. A.a and b show respectively intensity images measured by Alice (pixels $\mathbf{k} = (k_x < 0, k_y)$) and Bob (pixels $\mathbf{k} = (k_x > 0, k_y)$). These images do not provide any information about the correlation between photon pairs. Fig. A.c is the conditional image $\Gamma(\mathbf{k}, \mathbf{k_1})$ that represents the probability of measuring a photon from a pair at pixel $\mathbf{k}$ in Alice side conditioned by the detection of its twin photon at pixel $\mathbf{k_1}$ in Bob side. We observe a strong peak of correlation centred around the symmetric pixel $-\mathbf{k_1}$ due to the strong anti-correlation between momentum of the pairs (zoom in inset). Similarly, Fig. A.d is the conditional image $\Gamma(\mathbf{k}, \mathbf{k_2})$ relative to position $\mathbf{k_2}$. In this last case, the peak of correlation is very weak (zoom in inset). Finally, Fig. A.e shows the intensity correlation image

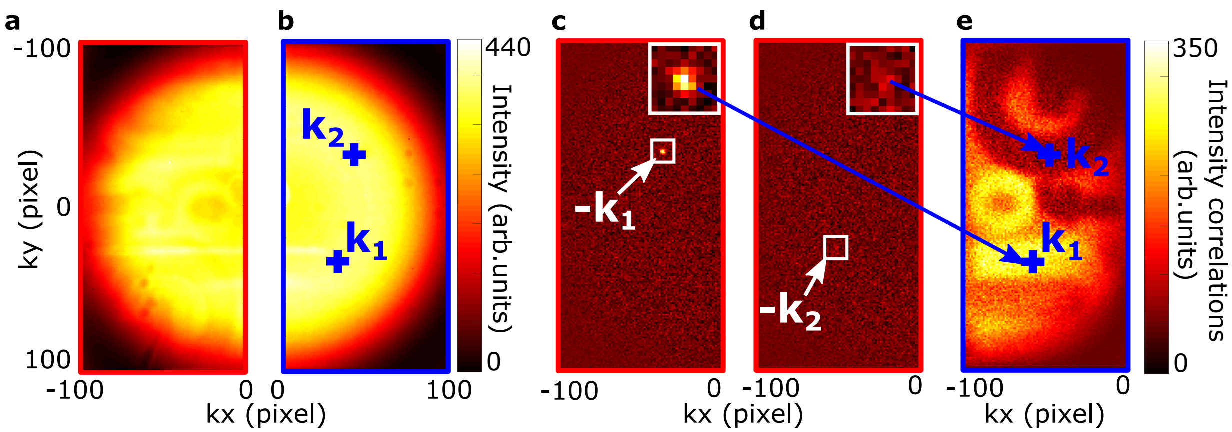

Figure A: ***Intensity and intensity correlation measurements between photon pairs with an EMCCD camera. a** and **b**, Intensity images measured respectively by Alice and Bob. Two pixels* $\mathbf{k_1}$ *and* $\mathbf{k_2}$ *are arbitrarily selected in Bob side.* ***c**, Conditional image relative to position* $\mathbf{k_1}$*.* ***d**, Conditional image relative to position* $\mathbf{k_2}$*. Zooms of areas centred around pixels* $-\mathbf{k_1}$ *and* $-\mathbf{k_2}$ *are shown in inset.* ***e**, Intensity correlation image reconstructed by Bob. Values at* $\mathbf{k_1}$ *and* $\mathbf{k_2}$ *correspond to intensity correlation values measured at* $-\mathbf{k_1}$ *and* $-\mathbf{k_2}$ *in images **c** and **d**.*

$R(\mathbf{k}) = \Gamma(\mathbf{k}, -\mathbf{k})$. In this last image, the value at pixel $\mathbf{k_1}$ corresponds to the value of the peak of correlation at $-\mathbf{k_1}$ shown in Fig. A.c and the value at pixel $\mathbf{k_2}$ corresponds to the value of the peak of correlation at $-\mathbf{k_2}$ in Fig. A.d.

2 Details on spatial and polarisation entanglement of the source

As described in Fig.3 of the manuscript, entangled photon pairs are generated by type I SPDC using a pair of BBO crystals. These pairs are entangled in both their polarisation and spatial degree of freedom [2].

Spatial entanglement Spatial entanglement between photons is characterised by performing intensity correlation measurement between (a) positions and (b) momentum of photons [3–5]. Fig. C describes the corresponding experimental apparatus:

(a) Positions $\mathbf{r}$ of photons are mapped onto pixels of the camera using a two-lens imaging configuration $f_1 - f_2$. After measuring the intensity correlation distribution $\Gamma(\mathbf{r_1}, \mathbf{r_2})$, its projection along the minus-coordinate axis $\mathbf{r_1} - \mathbf{r_2}$ is shown in Fig. C.b. The peak of correlation at its center is a signature of strong correlations between positions of photons. The position correlation width in the camera plane $\sigma_r^{(c)} = 26.20 \pm 0.02\mu\text{m} \approx 1.6$ pixel is estimated by fitting the minus-coordinate projection by a Gaussian model [6] of the form $a \exp(-|\mathbf{k_1} + \mathbf{k_2}|^2/(2\sigma_k^{(c)^2})$. To obtain a better estimate of the correlation width taking into account the approximation made by using the Gaussian model, a correction factor $\beta = \sqrt{\alpha/(\alpha + \alpha^{-1})}$ with $\alpha = 0.455$ [7,8] is applied to the measured width resulting into $\sigma_r = \beta\sigma_r^{(c)} = 10.85 \pm 0.06$ µm. Note that the use of such correction procedure is not crucial in our work because an overestimated value of the product $\sigma_k \sigma_r^{(c)} = [3.71 \pm 0.01].10^{-2} < \frac{1}{2}$ still violates significantly the EPR-type inequality [3].

(b) Momentum $\mathbf{k}$ of photons are mapped onto pixels of the camera by replacing the lens f_2 by a lens with twice its focal length. After measuring the intensity correlation distribution $\Gamma(\mathbf{k_1}, \mathbf{k_2})$, its projection along the sum-coordinate axis $\mathbf{k_1} + \mathbf{k_2}$ is shown in Fig. C.c. The peak of correlation at its center is a signature of strong anti-correlations between momentum of photons. The momentum correlation width in the camera plane $\sigma_k^{(c)} = 17 \pm 0.01\mu\text{m} \approx 1.1$

pixel is estimated by fitting the sum-coordinate projection by a Gaussian model [6] of the form $a\exp(-|\mathbf{k_1}+\mathbf{k_2}|^2/(2\sigma_k^{(c)^2})$. The corresponding value in the momentum space σ_k is then calculated using the formula $\sigma_k = 2\pi\sigma_k^{(c)}/(\lambda f_2) = [1.326 \pm 0.001] \times 10^3\,\text{rad.m}^{-1}$ where $f_2 = 100\text{mm}$ and $\lambda = 810\text{nm}$.

The presence of spatial entanglement between photons is certified by violating an EPR-type inequality: $\sigma_r\sigma_k = [1.44 \pm 0.01] \times 10^{-2} < \frac{1}{2}$ [3].

Polarisation entanglement The presence of polarisation entanglement between photons can be demonstrated by violating the Clauser-Horne-Shimony-Holt (CHSH) inequality [9]. A simplified version of the experimental apparatus used to perform this measurement is shown in Fig. C.d. In this case, the combination of Alice and Bob SLMs with a 45 degrees polariser positioned in front of the cameras play the role of the rotating polarisers used in a conventional CHSH violation experiment [10]. When a constant phase θ_B (θ_A) is programmed onto Bob SLM (Alice SLM), each pixel of Bob camera (Alice) performs a measurement that corresponds to an operator of the form:

$$\hat{B}_{\theta_B} = \frac{1}{2}[|H\rangle\langle H| + |V\rangle\langle V| + e^{i\theta_B}|H\rangle\langle V| + e^{-i\theta_B}|V\rangle\langle H|] \quad (3)$$

In the first step of this experiment, Alice and Bob measure intensity correlation images R_{θ_A,θ_B} for 16 combinations of phase values θ_A and θ_B programmed on their SLMs. On the one hand, Bob uses the same set as the one used in the holographic process $\theta_B = \{0, \pi/2, \pi, 3\pi/2\}$, where $\theta_B = 0$ and $\theta_B = \pi$ correspond to measurements performed in the diagonal polarisation basis $\hat{B}^{\pm}_{0/\pi} = (|V\rangle \pm |H\rangle)(\langle V| \pm \langle H|)$ and values $\theta_B = \pi/2$ and $\theta_B = 3\pi/2$ correspond to measurements performed in the circular polarisation basis $\hat{B}^{\pm}_{\frac{\pi}{2}/\frac{3\pi}{2}} = (|V\rangle \pm i|H\rangle)(\langle V| \mp i\langle H|)$. On the other hand, Alice programs phase values $\theta_A = \{\pi/4, 3\pi/4, 5\pi/4, 7\pi/4\}$ of her SLM to perform measurements in diagonal and circular basis rotated by $\pi/4$: $\hat{A}^{\pm}_{\frac{\pi}{4}/\frac{5\pi}{4}} = (|V\rangle \pm \frac{1}{\sqrt{2}}|H\rangle)(\langle V| \pm \frac{1}{\sqrt{2}}\langle H|)$ and $\hat{A}^{\pm}_{\frac{3\pi}{4}/\frac{7\pi}{4}} = (|V\rangle \pm \frac{i}{\sqrt{2}}|H\rangle)(\langle V| \mp \frac{i}{\sqrt{2}}\langle H|)$. Coincidence images associated with these $4 \times 4 = 16$ measurement combinations are shown in Figure B. In the second step, Alice and Bob combine these 16 intensity correlation images to compute E_{θ_A,θ_B} using the following formula [9]:

$$E_{\theta_A,\theta_B} = \frac{R_{\theta_A,\theta_B} - R_{\theta_A,\theta_B+\pi} - R_{\theta_A+\pi,\theta_B} + R_{\theta_A+\pi,\theta_B+\pi}}{R_{\theta_A,\theta_B} + R_{\theta_A,\theta_B+\pi} + R_{\theta_A+\pi,\theta_B} + R_{\theta_A+\pi,\theta_B+\pi}} \tag{4}$$

Finally, an image of S values is obtained using the following equation:

$$S = |E_{\pi/2,\pi/4} - E_{\pi/2,5\pi/4}| + |E_{0,\pi/4} + E_{0,5\pi/4}| \tag{5}$$

This image is shown in Fig.5.b of the manuscript and in Fig. C.e. We observe that 10789 values of S measured between in Alice and Bob correlated pixels show violation of the CHSH inequality $S > 2$, over the total of 14129 within the two half-disks. A spatial averaged value of $\langle S \rangle = 2.20 \pm 0.003 > 2$ is estimated by calculating the mean of S values over the two half-disks areas, and the error on $\langle S \rangle$ is calculated from their variance. Violation of CHSH inequality demonstrates the presence of polarisation entanglement between photon pairs.

3 Details on signal-to-noise and spatial resolution

This section provides more details about the signal-to-noise ratio (SNR) and spatial resolution of the phase image retrieved by quantum holography.

Signal-to-noise ratio. In our work, we define the SNR as the ratio between π and the standard deviation of the noise measured in a region of the image in which phase values equal π. It is

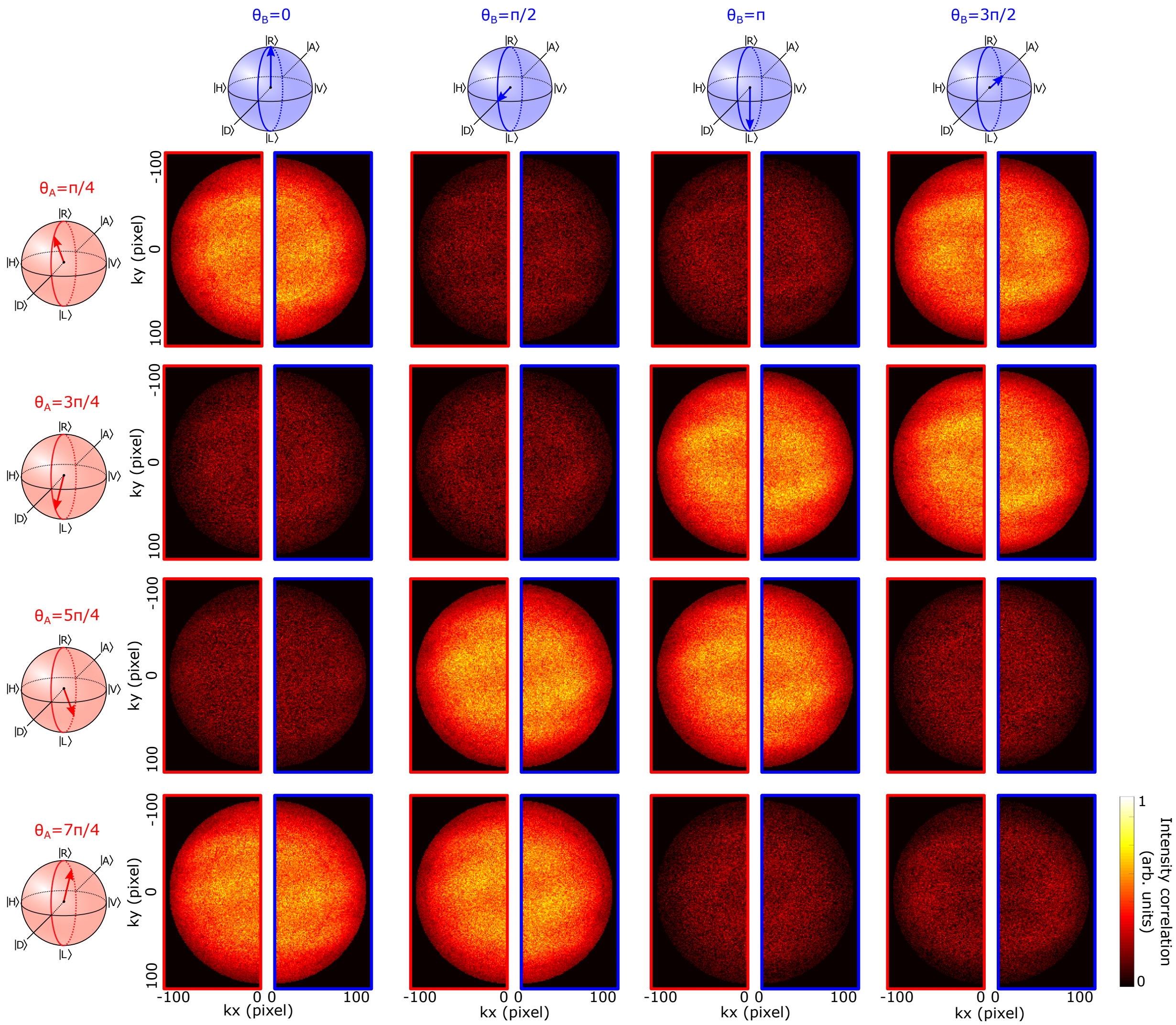

Figure B: ***Intensity correlation images measured by Alice and Bob for*** 16 ***combinations of phase values*** θ_A ***and*** θ_B***.*** *Intensity correlation images are shown by pair, with a red outline for Alice and a blue outline for Bob. Each row corresponds to a measurement setting on Alice SLM* $\theta_A = \{\pi/4, 3\pi/4, 5\pi/4, 7\pi/4\}$ *and each column to a measurement setting of Bob SLM* $\theta_B = \{0, \pi/2, \pi, 3\pi/2\}$.

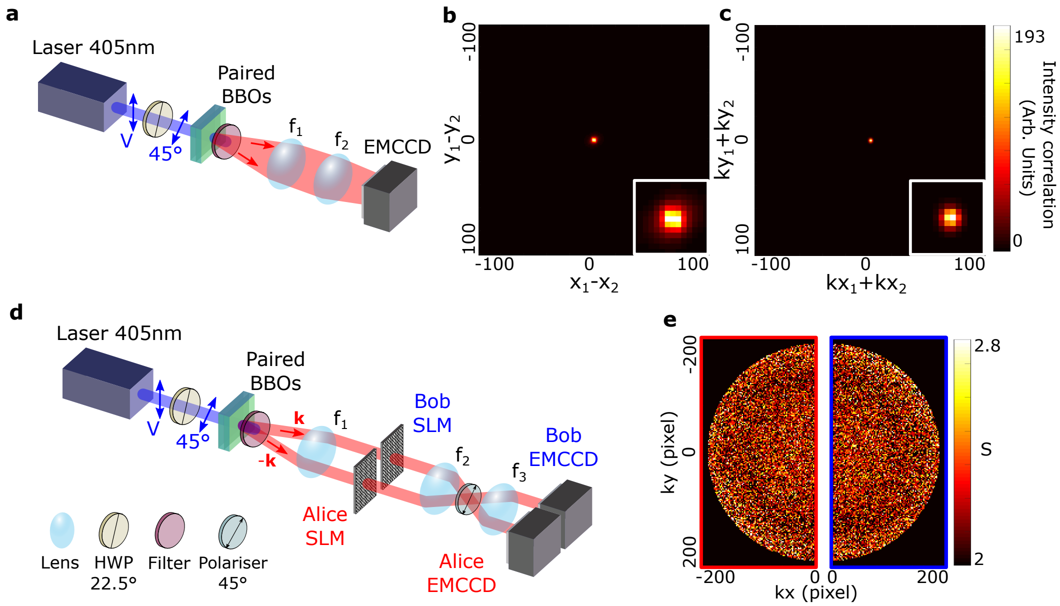

Figure C: ***Spatial and polarisation entanglement characterisation. a****, Experimental setup used for spatial entanglement characterisation. $f_1 = 75$mm and $f_2 = 100$mm form a two-lenses imaging system.* ***b****, Minus-coordinate projection of the intensity correlation distribution measured between positions of photons. Zoom of the central area is in inset. The width of the peak $\sigma_r^{(c)} = 26.20 \pm 0.02\mu$m is measured using a Gaussian model of the form $a \exp(-|\mathbf{x_1} - \mathbf{x_2}|/(2{\sigma_r^{(c)}}^2))$.* ***c****, Sum-coordinate projection of the intensity correlation distribution measured between momentum of photons. In this case, the lens f_2 is replaced by a lens of twice smaller focal length $f_2' = 50$mm to map momentum of photons onto pixels of the camera. Zoom of the central area is in inset. The width of the peak $\sigma_k^{(c)} = 17.00 \pm 0.01\mu$m is measured using a Gaussian model of the form $a \exp(-|\mathbf{k_1} + \mathbf{k_2}|/(2{\sigma_r^{(c)}}^2))$.* ***d****, Experimental setup used for polarisation entanglement characterisation. $f_1 = 54$mm is positioned in a Fourier imaging configuration and $f_2 = 150$ and $f_3 = 100$mm for a two-lenses imaging configuration.* ***e****, Image of measured Clausen-Horne-Shimony-Holt (CHSH) inequality values, denoted S.*

for example the case for the area within the letters U and o in the phase image shown in Fig.1.b. For a constant source intensity and a fixed exposure time, the factor that most influences the SNR is the total number of images N acquired to measure the four intensity correlation images used to reconstruct the phase image. Each phase image shown in the manuscript has been retrieved using $N = 2.5 \times 10^6$ images and show SNR values ranging between 19 and 21. Fig.D.a shows SNR values measured for different values of N (black crosses). As predicted by the theory [1] and demonstrated by fitting the data (blue dashed curve), the SNR evolves as $\sqrt{N}$. Fig.D.b-c show three images of the retrieved phase for respectively $N = 2.5 \times 10^4$ images, $N = 2.5 \times 10^5$ and $N = 2.5 \times 10^7$ images.

Spatial resolution. To measure the spatial resolution in the retrieved phase image, a radial resolution target (Siemens star with 16 branches) is programmed by Alice Fig. D.e. Fig. D.f shows the retrieved image. When comparing this retrieved image (Fig. D.f) to the ground truth (Fig. D.e), the area of the resolution target that is not spatially resolved is approximately a disk of diameter 29 pixels, which corresponds to a perimeter of 91 pixels. The spatial resolution is then estimated by dividing the perimeter by twice the number of branches $91/(2 * 16) \approx 2.8$ pixels, which results to a spatial resolution of $d = 45 \pm 3$ µm. We observe that this value of the spatial resolution is larger than this of the momentum correlation width ($\sigma_k = 18$µm on the camera, see Fig. C) which in theory should be the resolution limit of our system. The origin of this difference is that the SLM on which phase objects are programmed is not perfectly positioned into an image plane of the system, which is a misalignment that can be expected when using an SLM acting in reflection and tilted. This misalignment causes a small blurring of the phase object programmed on the SLM and thus lead to an overestimation of the measured value of the spatial resolution width.

4 Details on phase distortion characterisation

This section provides more details about the characterisation of the phase distortion Ψ_0.

Phase distortion $\Psi(\mathbf{k})$ originates from the SPDC process used to produce pairs of photons [11,12]. To characterise it, Alice and Bob perform a quantum holographic experiment using the scheme described in Fig.1.a. In this case, Alice programs a flat phase pattern $\theta_A = 0$ (Fig. E.a) and Bob programs successive phase shifts patterns with values $+0$ (Fig. E.b), $+\pi/2$ (Fig. E.b), $+\pi$ (Fig. E.b) and $+3\pi/2$ (Fig. E.b), without any correction phase mask superimposed on them. Fig. E.f-i show intensity correlations images measured for each of the four SLM patterns displayed by Bob. Therefore, the resulting reconstructed phase image corresponds exactly to the phase distortion $\Psi_0(\mathbf{k})$ (Fig. E.j). The phase image is then fitted by a quadratic function of the form $\Psi_0(k_x, k_y) = 4.69k_x^2 + 5.04k_y^2 + 0.02$ (Fig. E.k). Result of the fit is then used to construct and program the phase compensation pattern on Bob SLM (Fig. E.l).

5 Details on quantum holography without polarisation entanglement

This section provides more details about quantum holography performed with photons entangled in space but not in polarisation.

Fig.2 of the manuscript shows results of quantum holographic experiment performed with

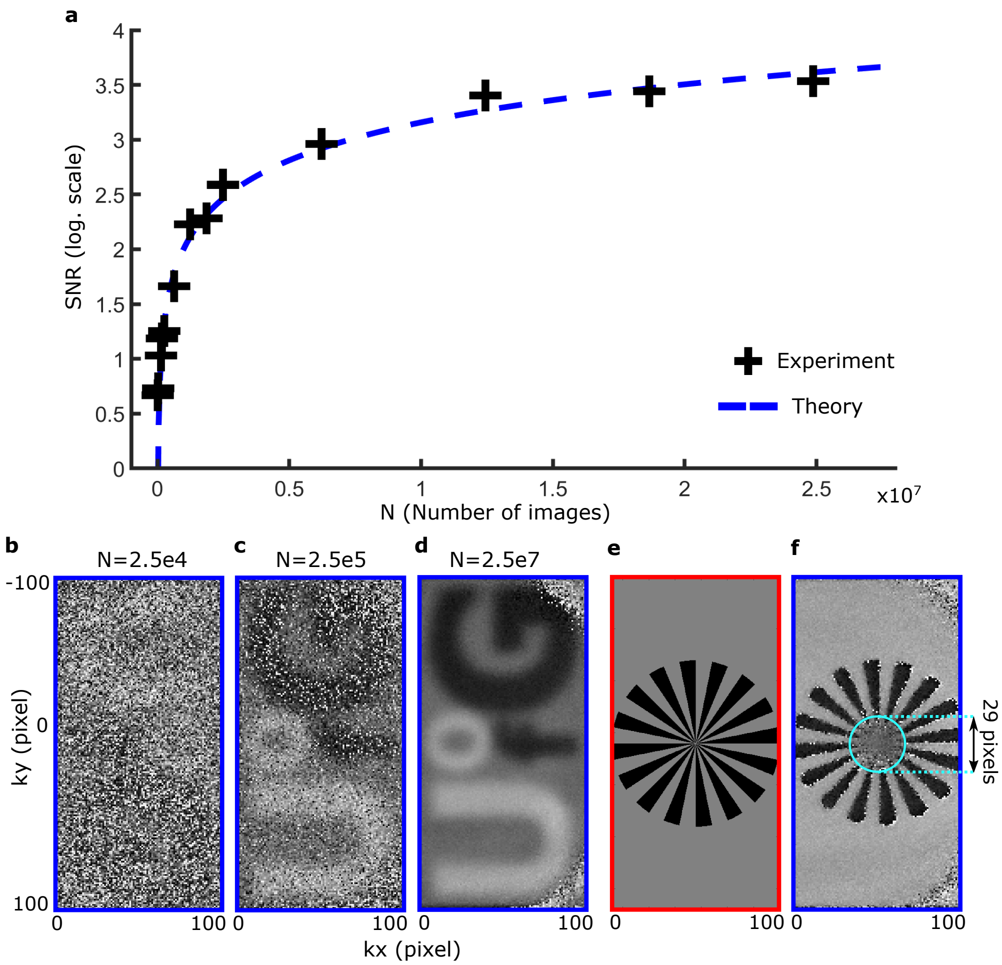

Figure D: ***Signal-to-noise and spatial resolution*.** ***a***, *Values of single-to-noise ratio (SNR) in the retrieved phase image measured for different total number of images acquired* N *(black crosses) together with a theoretical fit of the form: SNR=* $0.074\sqrt{N}$ *(blue dashed line).* ***b***, *Phase image reconstructed using* $N = 2.5 \times 10^4$ *images.* ***b***, *Phase image reconstructed using* $N = 2.5 \times 10^5$*images.* ***b***, *Phase image reconstructed using* $N = 2.5 \times 10^7$*images.* ***e***, *Radial resolution target (Siemens star with 16 branches) phase pattern programmed on Alice SLM.* ***f***, *Reconstructed phase image of the radial resolution target. Resulting spatial resolution is* $d = 45 \pm 3$ μ*m, which corresponds to approximately to* 2.8 *pixels*

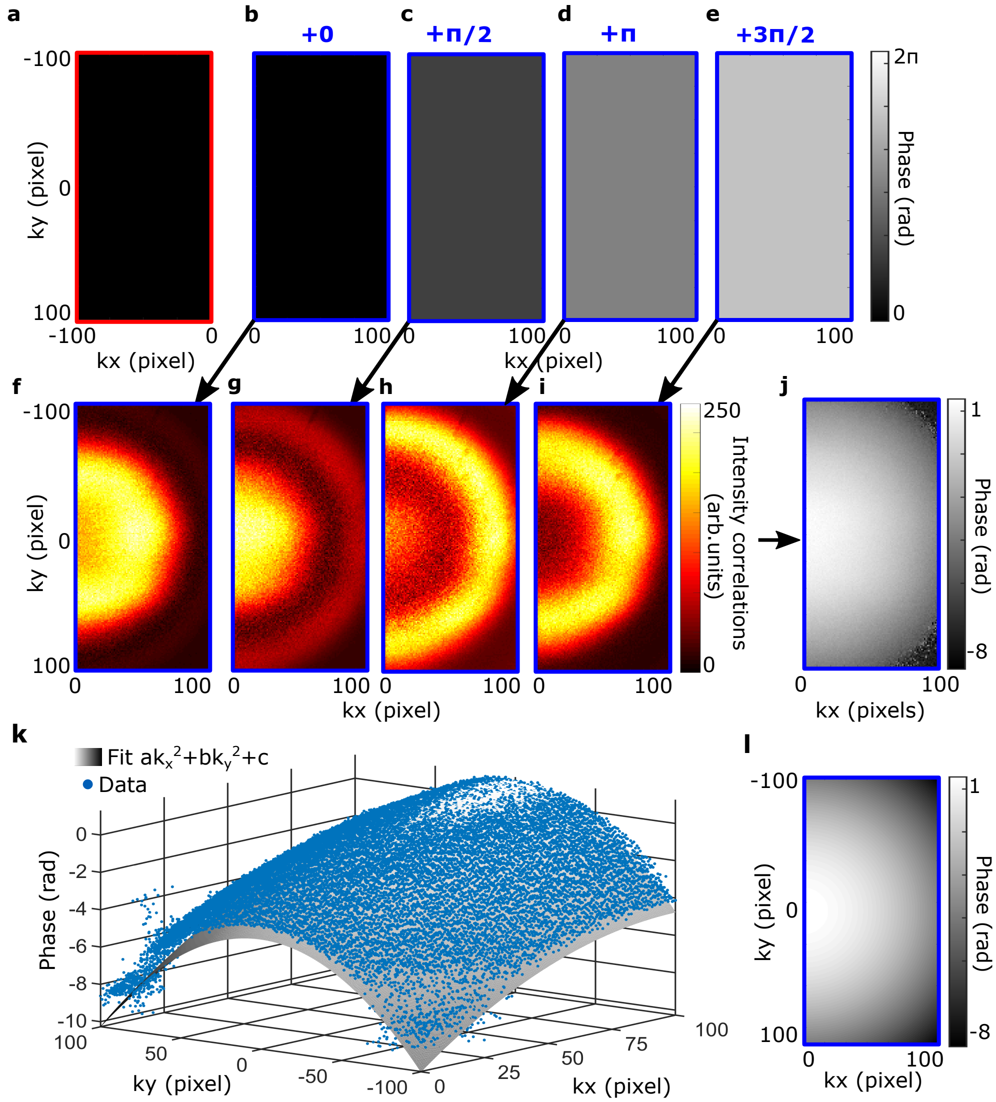

Figure E: ***Phase distortion characterisation. a***, *Flat phase pattern programmed on Alice SLM.* ***b-e***, *Phase-shifted patterns programmed on Bob SLM:* $+0$ (***b***), $+\pi/2$ (***c***), $+\pi$ (***d***) *and* $+3\pi/2$ (***e***). ***f-i***, *Intensity correlation images measured for each phase mask displayed on Bob SLM.* ***j***, *Phase image retrieved by Bob.* ***k***, *Fit of the phase image by a quadratic function of the form:* $\Psi_0(k_x, k_y) = 4.69k_x^2 + 5.04k_y^2 + 0.02$. ***l***, *Correction phase pattern resulting from the fitting process.*

photons that are entangled in space but not in polarisation. In this experiment, the state generated at the output of the crystals is defined by the density operators:

$$\frac{1}{2}\sum_{\mathbf{k}}\left[|H\rangle_{\mathbf{k}}|H\rangle_{-\mathbf{k}}\langle H|_{\mathbf{k}}\langle H|_{-\mathbf{k}}+|V\rangle_{\mathbf{k}}|V\rangle_{-\mathbf{k}}\langle V|_{\mathbf{k}}\langle V|_{-\mathbf{k}}\right] \tag{6}$$

This state is composed of a balanced statistical mixture of two pure states: $\sum_{\mathbf{k}}|H\rangle_{\mathbf{k}}|H\rangle_{-\mathbf{k}}$ and $\sum_{\mathbf{k}}|V\rangle_{\mathbf{k}}|V\rangle_{-\mathbf{k}}$. As shown in Fig. F.a, this state is produced by alternating the polarisation of the pump laser between vertical and horizontal polarisations. Frames acquired by the camera in each configuration are then summed together (Fig. F.b). Then, the intensity and intensity correlation images shown in Fig.2 of the manuscript are reconstructed using the set of summed frames. This experiment is equivalent of generating the photons with a pump that is coherent in space and time but not in polarisation (i.e. unpolarised). Due to the fundamental transfer of coherence that occurs between the pump and the down-converted two-photon field in SPDC [13–15], the produced state is entangled in space and time, but not in polarisation.

Note that, even if entanglement is absent, we still observe some small spatial inhomogeneities in the reconstructed phase in the Figure.2.d of the manuscript. These inhomogeneities originate from the small spatial variations observed in the corresponding intensity correlation images (Figs.2.f-i of the manuscript), that themselves originate from the small and not desired intensity modulations performed by the SLM during the phase shifting process. This effect is also present in the measurements performed with polarisation entanglement, but it is not visible in the reconstructed phase (Fig.1.j) because the corresponding spatial variations in intensity correlations images (Figs.1.f-i) are negligible compared to those created by the object.

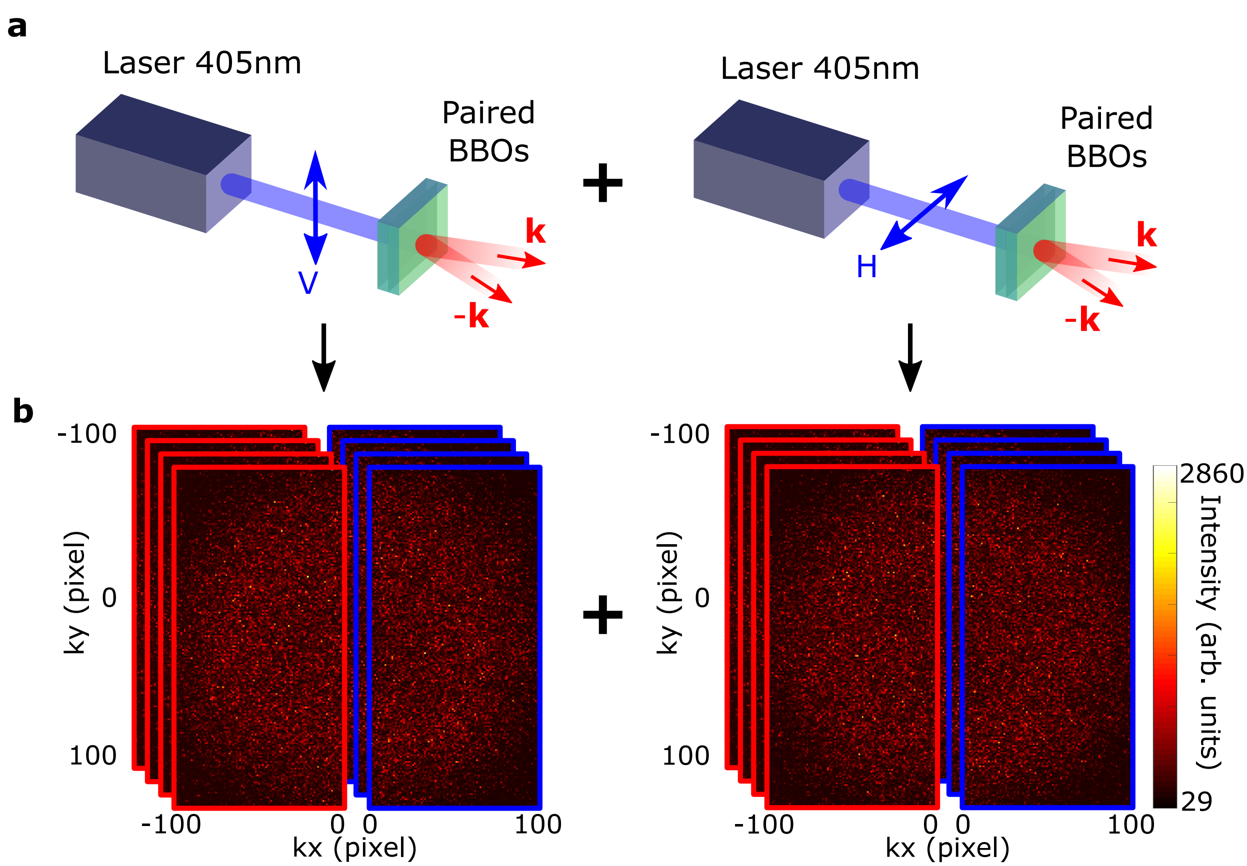

Figure F: ***Generation of a mixed state without polarisation entanglement. a****, Experimental configurations used to generate the mixed state:* $\sum_{\mathbf{k}} [|H\rangle_{\mathbf{k}}|H\rangle_{-\mathbf{k}}\langle H|_{\mathbf{k}}\langle H|_{-\mathbf{k}} + |V\rangle_{\mathbf{k}}|V\rangle_{-\mathbf{k}}\langle V|_{\mathbf{k}}\langle V|_{-\mathbf{k}}]$. *Polarisation of pump laser is alternated between vertical and horizontal.* ***b****, Frames acquired in each configuration are summed. Intensity images shown in Fig.2.b.c of the manuscript and intensity correlation images shown in Fig.2.e-f of the manuscript are reconstructed from the set of summed frames.*

6 Details on the characterisation of the dynamic phase disorder

This section provides more details about the dynamic phase disorder and its characterisation.

Fig. G.a shows the experimental setup used to characterise properties of the phase disorder introduce by the presence of the diffuser, that is a plastic sleeve layer of thickness < 100 µm. Without diffuser, a sine-shaped phase image programmed on the SLM (Fig. G.b) generates a very specific diffraction pattern on the camera (Fig. G.c). After introducing the static diffuser, the diffraction pattern becomes a speckle pattern (Fig. G.c). The presence of the diffuser erases all information about the phase image, that cannot be retrieved by classical holographic techniques such as phase retrieval [16] and phase-stepping holography [17]. When the diffuser is moving, the speckle pattern takes the form of a diffuse halo if the exposure time of the camera is larger (0.5s) than the typical decorrelation time of the speckle. The halo width is estimated to 1.3mm by Gaussian fitting which corresponds approximately to a diffusing angle of 1 degree and a surface roughness of 46 µm. Moreover, the dynamic properties of the disorder are estimated by measuring the speckle decorrelation time. Speckle correlation coefficients are calculated by acquiring a series of speckle patterns using short exposure times (3ms) and correlating them with a reference speckle image. Fig. G shows the decrease of speckle correlation with time (black crosses). A typical decorrelation time of 183ms is measured by fitting data with an exponential model (dashed blue curve).

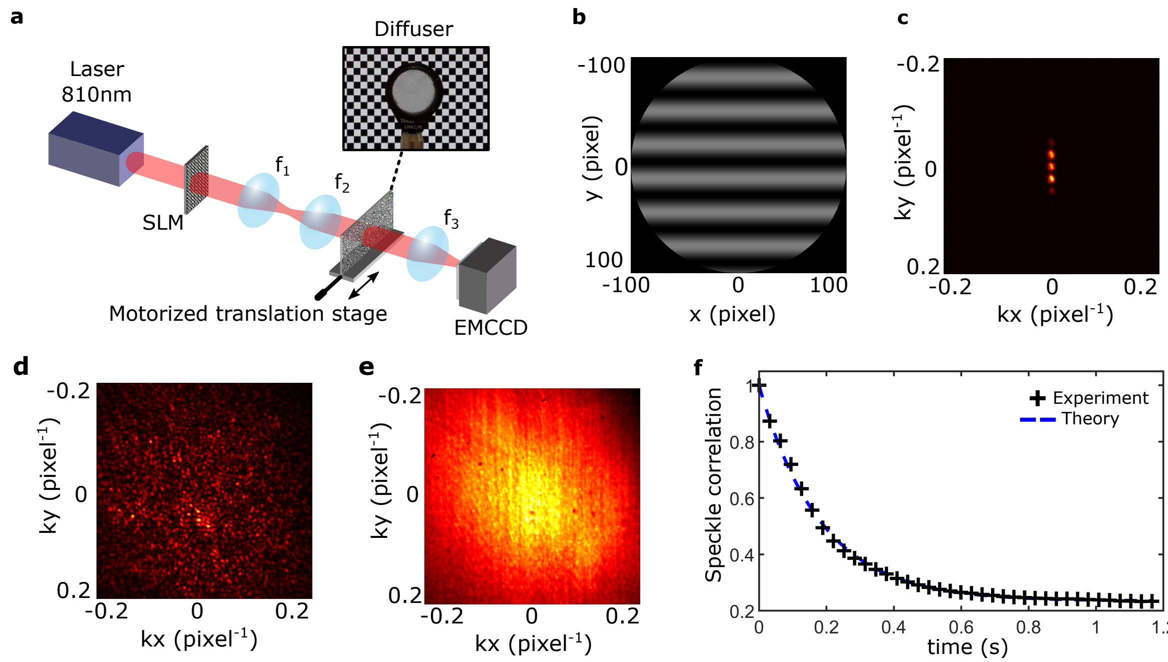

Figure G: ***Characterisation of the dynamic phase disorder***. ***a***, *A classical laser (*$810nm$ *; beam diameter* $0.8mm$*) illuminates an SLM that is imaged onto a the diffuser by two lenses* $f_1 = 150mm$ *and* $f_2 = 75mm$*. Lens* $f_3 = 75mm$ *Fourier-images the diffuser onto the camera.* ***b***, *Sine-shaped phase pattern programmed on the SLM.* ***c***, *Intensity image measured on the camera without diffuser.* ***d***, *Intensity image measured on the camera with the diffuser maintained static.* ***e***, *Intensity image measured on the camera with the moving diffuser using an exposure time of* $0.5s$*. Width of the diffuse halo is estimated to* $1.3mm$ *by fitting with a Gaussian function.* ***f***, *Measurement of speckle correlation values with time (black crosses) together with a theoretical fit of the form* $1 - 0.77(1 - e^{-t/0.183})$ *(blue dashed line). Typical decorrelation time equals to* $183ms$*.*

7 Details about the quantum holographic measurements performed in the presence of static and dynamic stray light

This section provides more details about the quantum holographic measurements performed in the presence of stray light.

Figure H and I show experimental results of quantum holographic measurements performed with dynamic and static stray light falling on the sensor, respectively. Figures H.a,c,d and g are respectively the same images than those shown in Figure 4.e-h of the manuscript. In addition, Figure H.e and f show intensity images acquired by Alice and Bob in the presence of the same stray light but maintained static on purpose to show the complex spatial shape of the time-varying speckle pattern. Figure H.b show the phase image reconstructed without stray light (SNR=12 and NMSE=6%) and Figures H.h shows the phase image reconstructed in the presence of dynamic stray light with intensity ratio quantum/classical of 1.2. Furthermore, Figures I.i-m show the four intensity correlation images used for reconstructing the phase image in the case of the presence of dynamic stray light with ratio 0.5. No traces of classical stray light appear on any the intensity correlation images [18], while they are well visible on the direct intensity images (Figs. H.c.d). For comparison, Fig. Hi shows a very degraded phase image (NMSE=82%) retrieved using an equivalent classical holographic system (see Figure K.b), under the same dynamic stray light conditions with intensity ratio of 0.5 (see Methods). To confirm that the absence of classical traces is not due to a spatial averaging effect by the time-varying speckle, we performed the same experiment with static stray light. Figure Ia shows a scheme of the experimental setup including the static stray light i.e. two cat-shaped objects illuminated by a classical laser. Figures I.b-e show the reconstruction of a phase image in the presence of two cat-shaped images superimposed on Alice and Bob sensors. Figures I.f-i confirm the absence of classical traces on the intensity correlation images used to reconstruct the phase. This additional experiment confirms that our quantum holographic protocol is insensitive to the dynamics of stray light.

We characterise the SNR variation in function of the average intensity of classical light falling on the sensor using a similar approach reported elsewhere [18]. We use the experimental setup described in Fig.3 of the manuscript without the random phase disorder and with no phase object programmed on the SLM. Intensity correlation measurements are then performed for different classical stray light average intensity values $\langle I_{cl} \rangle$, with a constant quantum illumination intensity $\langle I_{qu} \rangle$. These intensity correlation measurements are visualized by projecting them onto the sum-coordinate axis [4,5]. For example, Fig. J.d and e show images of intensity correlation measurements in the sum-coordinate basis in the presence of classical stray light with an average intensity ratios of $\langle I_{cl} \rangle / \langle I_{qu} \rangle = 0$ and $\langle I_{cl} \rangle / \langle I_{qu} \rangle = 5.4$, respectively. The bright peaks at the center of the images are signatures of the strong momentum anti-correlation between the pairs. The peak value is proportional to the mean value of an intensity correlation image measured in the same conditons (i.e.*signal* of the SNR). The standard deviation of noise in the pixels surrounding the peak is proportional to the standard deviation of the noise in an intensity correlation image acquired in the same conditions (i.e. *noise* of the SNR). The SNR values shown in Fig J.a are calculated by dividing peak values by standard deviations for different values of $\langle I_{cl} \rangle / \langle I_{qu} \rangle$. Fitting these experimental results with a theoretical model described in [19] shows that the SNR varies as $1/\langle I_{cl} \rangle$.

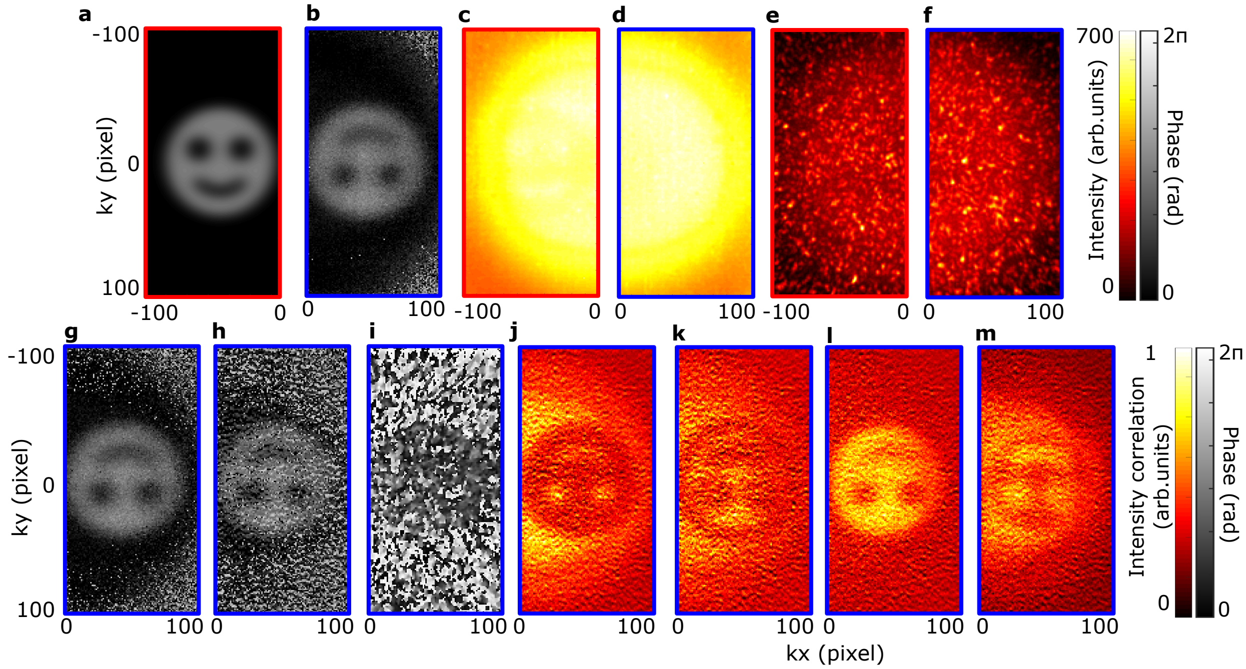

Figure H: ***Phase reconstruction through dynamic stray light.*** ***a****, Phase image programmed by Alice.* ***b****, Phase image reconstructed by Bob without stray light (SNR=*12 *and NMSE=*6%*).* ***c*** *and* ***d****, Intensity images measured by Alice and Bob in the presence of dynamic stray light, respectively.* ***e*** *and* ***f****, Intensity images measured by Alice and Bob in the presence of the same stray light but maintained static on purpose to show the complex spatial structure of the time-varying speckle pattern.* ***g*** *and* ***h****, Phase images retrieved by Bob with dynamic stray light of average intensity* 0.5 *that of quantum light (SNR=*9 *and NMSE=*17%*) and dynamic stray light with intensity* 1.2 *that of quantum light (SNR=*3 *and NMSE=*43%*), respectively.* ***i****, Phase image reconstructed using an equivalent classical holographic system under similar dynamic stray illumination conditions with* 0.5 *average intensity ratio (NMSE=*82%*) (see Figure K.b)* ***j-m****, Intensity correlation images measured for each phase shifting mask displayed on Bob SLM, with no traces of classical stray light (intensity ratio* 0.5*). All images were reconstructed from* 5×10^6 *frames.*

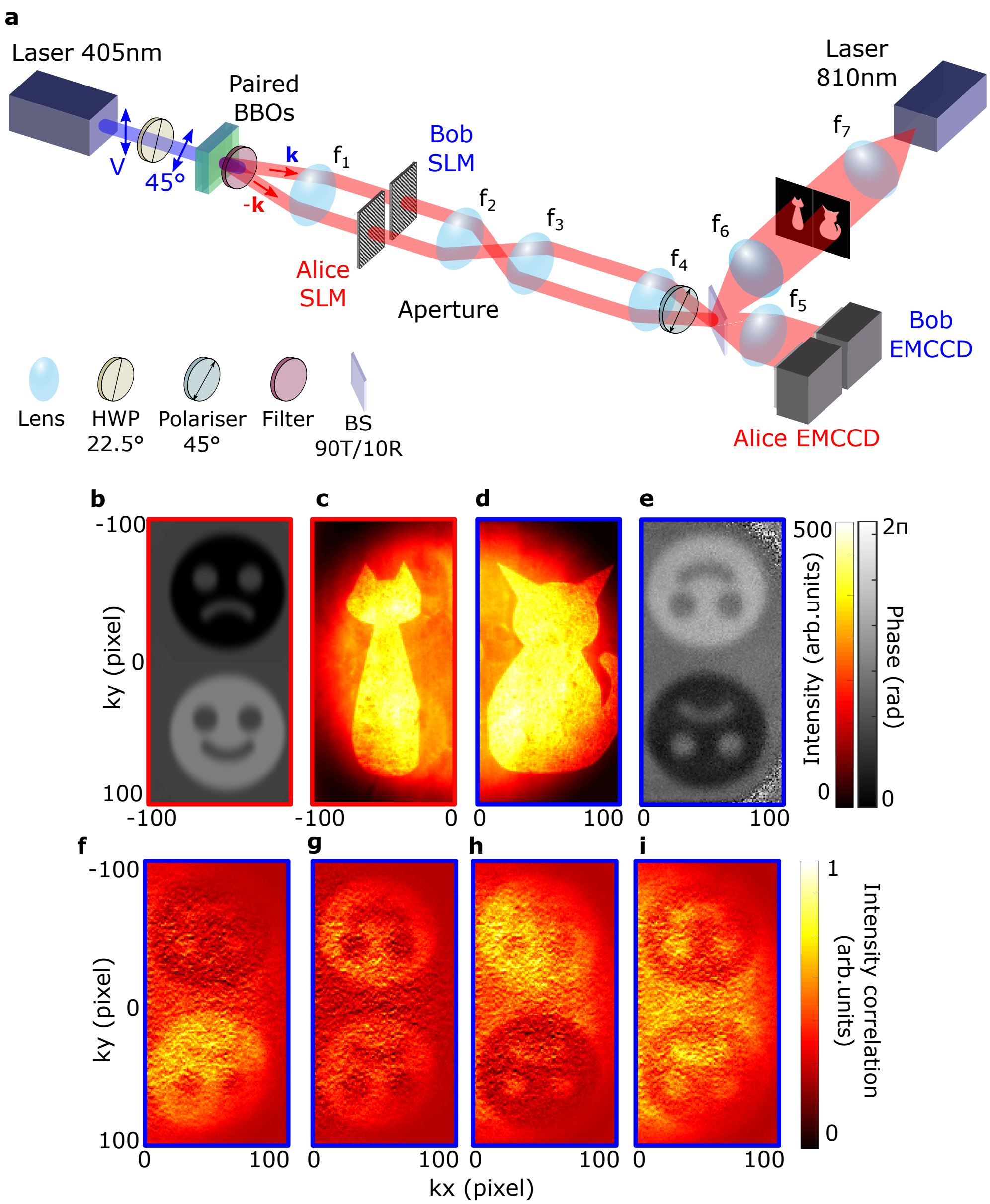

Figure I: ***Phase reconstruction through static stray light.*** *Experimental setup including the source of static stray light i.e. two cat-shaped objects illuminated by a classical laser.* ***b****, Phase image encoded by Alice.* ***c*** *and* ***d****, Intensity images measured by Alice and Bob with well visible cat-shaped images.* ***e****, Phase image retrieved by Bob with SNR$=20$ and NMSE$=5\%$.* ***f-i****, Intensity correlation images measured for each phase mask displayed on Bob SLM, with no traces of cat-shaped classical images. The phase image was reconstructed from 5.10^6 frames.*

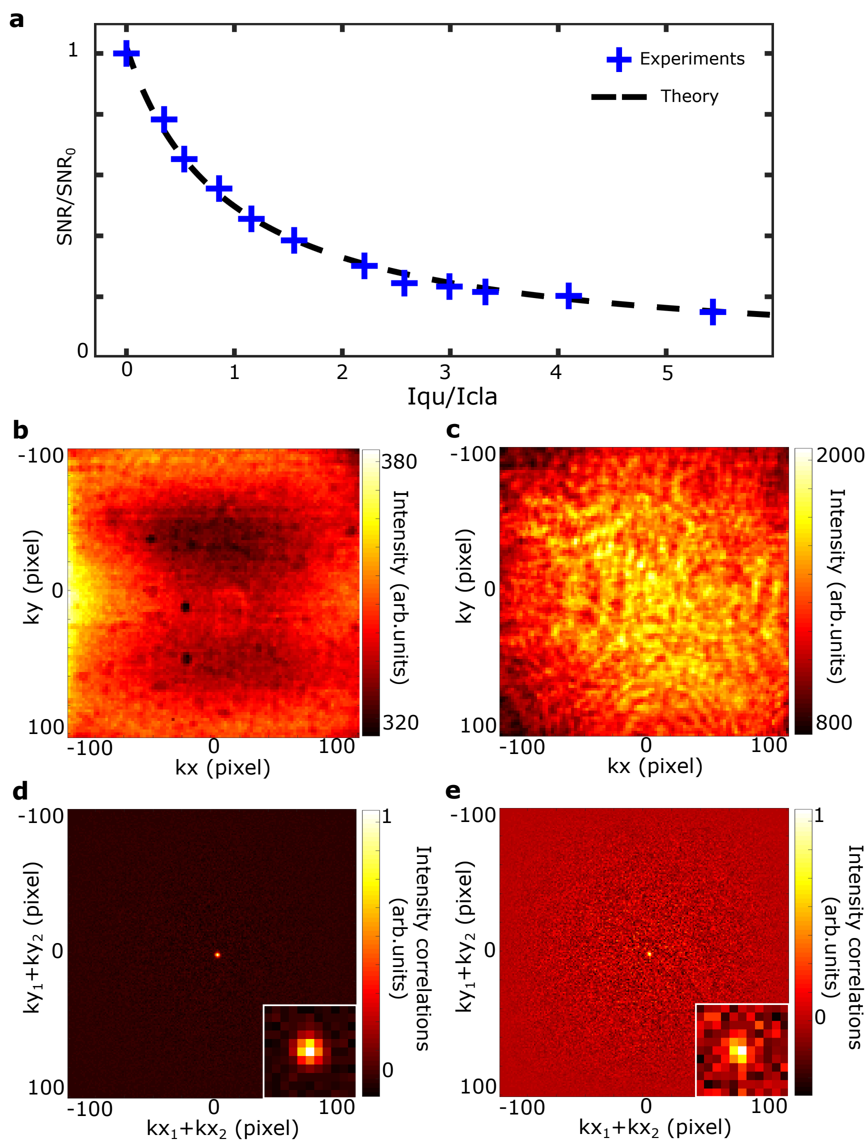

Figure J: ***SNR variation in the presence of stray light.*** ***a****, Normalised SNR values in function of the average intensity ratio between classical and quantum illumination $\langle I_{cl}\rangle/\langle I_{qu}\rangle$.* ***b*** *and* ***c****, Intensity images measured for $\langle I_{cl}\rangle/\langle I_{qu}\rangle = 0$ and $\langle I_{cl}\rangle/\langle I_{qu}\rangle = 5.4$, respectively.* ***d*** *and* ***e****, Images of intensity correlation measurements represented in the sum-coordinate axis $\mathbf{k_1} + \mathbf{k_2}$ for $\langle I_{cl}\rangle/\langle I_{qu}\rangle = 0$ and $\langle I_{cl}\rangle/\langle I_{qu}\rangle = 5.4$, respectively. Insets are zooms of the central peak area.*

8 Details on the resolution enhancement characterisation

This section provides more details about the comparison of spatial resolution between classical and quantum holographic systems.

Various criteria can be used to compare spatial resolution of two imaging systems [20]. In our work, we chose to compare their spatial frequency cut-off. Figure K shows the experimental apparatus used to perform such analysis with the quantum holographic protocol (Figure K.a) and its classical version (Figure K.b). In these configurations, the Fourier plane of the SLM, that is also the plane of the aperture, is imaged onto the EMCCD camera. This is done by substituting the lens f_5 in the initial experimental setup described in Figure 3 of the manuscript by a lens of half focal length $f_5/2$. In the classical case, when a 26 pixel period phase grating (Fig. K.c) is programmed on the SLM (i.e. on Alice SLM in the quantum case), the intensity image shows a diffraction pattern with three main components: a central zero-order peak and two symmetrically positioned plus-or-minus first-order peaks (Fig. K.d). In the quantum case, intensity image does not reveal any specific diffraction pattern (Fig. K.e). To reveal the frequency content of the phase object under the quantum illumination, we perform intensity correlation measurements between all pair of pixels of the EMCCD camera and visualise these data by projecting them along the minus-coordinate axis $\mathbf{r_1} - \mathbf{r_2}$ [21,22]. Similarly to the classical case, we observe three peaks of intensity correlations in Fig. K.e. When the same experiment is reproduced with a 16 pixels period grating (Fig. K.g), the first-order diffraction peak is blocked by the aperture in the classical case (Fig. K.h), while it remains present under quantum illumination (Fig. K.j). In Fig.5.b of the manuscript, red circles and blue crosses are values of (plus) first-order peak intensities measured for different grating periods in the classical and quantum case, respectively.

The use of spatially entangled photon pairs to enhance the resolution of an imaging system compared to its classical coherent version was previously demonstrated [23]. This effect can be understood using a simple theoretical model [24]. First, we assume that the crystal is very thin and the pump beam diameter is infinite. In this case, the spatial component of the two-photon wavefunction can be written as:

$$\phi(\mathbf{r_1}, \mathbf{r_2}) = \delta(\mathbf{r_1} - \mathbf{r_2}) \tag{7}$$

where $\mathbf{r_1}$ and $\mathbf{r_2}$ are positions in the crystal plane. Then, we consider an object $t(\mathbf{k})$ positioned into one half of the Fourier plane of the crystal (i.e. illuminated by only one photon of the pair). The object is imaged onto another imaging plane through an imaging system with a coherent point spread function denoted $h(\mathbf{k})$. The intensity correlation image $R(\mathbf{k})$ obtained at the output can be written as:

$$R(\mathbf{k}) = \left| t * h^2 \right|^2 (\mathbf{k}) \tag{8}$$

where $*$ is the convolution product. In the classical case, the intensity image $I(\mathbf{k})$ obtained at the output is:

$$I(\mathbf{k}) = \left| t * h \right|^2 (\mathbf{k}) \tag{9}$$

Because the convolution kernel in the quantum case is squared compared to classical coherent light, the spatial resolution is enhanced by a factor 2. In the Fourier domain, this resolution enhancement corresponds a broadening of the optical transfer function and therefore an increase of

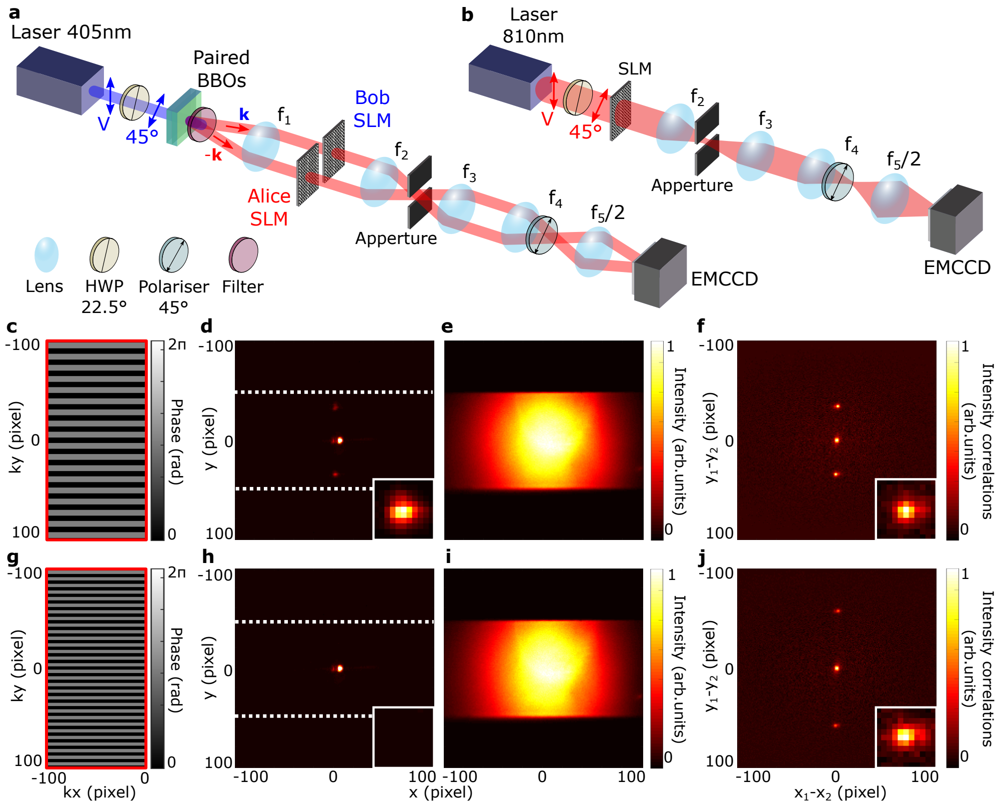

Figure K: ***Resolution enhancement characterisation. a*** *and* ***b****, Experimental apparatus used for spatial frequency cut-off measurement of the quantum and classical holographic systems, respectively.* ***c****,* 26 *pixels period phase grating programmed on the SLM (only Alice SLM in the quantum case).* ***d****, Intensity image measured with the classical system. Inset is a zoom on the first-order diffraction peak. White dashed lines represent the edges of the aperture.* ***e****, Intensity image measured in the quantum system.* ***f****, Projection of the intensity correlation matrix onto the minus-coordinate axis* $\mathbf{r_1} - \mathbf{r_2}$ *that shows three diffraction peaks. Inset is a zoom on the first-order diffraction peak.* ***g****,* 16 *pixels period phase grating programmed on the SLM.* ***h****, Intensity image measured with the classical system. First-order diffraction peaks are blocked by the aperture.* ***i****, Intensity image measured in the quantum system.* ***j****, Projection of the intensity correlation matrix onto* $\mathbf{r_1} - \mathbf{r_2}$ *that still shows three diffraction peaks.*

the corresponding spatial frequency cut-off [20]. Note that, because the crystal has in practice a finite thickness and the pump beam diameter is not infinite, the spatial resolution enhancement measured is lower than 2 (but higher than 1).

9 Details on the photon pair source, detection efficiency of the experimental setup and Allan variance plot

This section provides more details about the rate of generation of SPDC pairs, the detection efficiency of the setup and reports an Allan variance plot.

Rate of pair generation. To characterise the photon pair rate of the source, a threshold is applied on the EMCCD camera: in each acquired images, all grey values bellow 210 are set to 0 and all values above are set to 1. As detailed in [19], this approach turns the EMCCD into a multi-pixel photon counter with an effective quantum efficiency of 0.61. By acquiring a total of 7000 frames with an exposure time of 3ms (no pattern on the SLM and after removing the polarisers), we measure an average photon rate of 304 photons per second per pixel and an average number of pairs of 0.1 pairs per pixel per second (spatial mode = 1.1 pixels, as shown in Fig.C). The same experiment reproduced with the shutter closed returns 4.1 photons per pixel per second and 5.10^{-4} pairs per spatial mode per second, showing that the noise is negligible.

Detection efficiency of the experimental setup. Detection efficiency of the entire setup is estimated by multiplying the efficiency of each optical components. The SLM is an Holoeye Pluto NIR-II with a reflection efficiency of approximately 0.64 at 800nm. Lenses are all coated for

800nm, therefore their losses are negligible. Finally, the Andor Ixon Ultra EMCCD camera sensor has approximately 0.75 quantum efficiency (data sheet provided by Andor). The total detection efficient is therefore about $0.75 * 0.64 = 0.48$.

Allan deviation. Figure L shows an Allan deviation plot [25]. It is constructed from the successive measurement of $N = 50000$ intensity correlation images (flat SLM pattern), each measured from 622 frames, that is the size of the internal buffer of the camera. In our experiment, the 'time' domain signal denoted $R(t)$ is composed of the spatial averaged values (over an area of 100×100 pixels) of each intensity correlation image taken at an acquisition number $t \in [1, 50000]$ (i.e. the 'time' corresponds to the 'image set number'). To calculate the Allan deviation $\sigma(\tau)$ from $R(t)$, where τ is the averaging time, we used the method detailed in [26]. Figure L shows that the slope at small τ equals $-1/2$, meaning that our measurements are not shot-noise-limited (i.e.slope -1).

10 Quantum holographic imaging of real objects

Figure M shows results of quantum holographic imaging performed on two real objects, a piece of scotch tape and a bird feather. The objects are positioned on a microscope slide in place of Alice SLM. Spatial phase variations due to the stress-induced (scotch tape) and structural (bird feather) birefringence are clearly visible in the phase images reconstructed by Bob in Figs. M.c and g. Furthermore, we show that Bob can also retrieve the object amplitudes (Figs. M.d and h) from the same set of intensity correlation measurements by simply replacing the argument in equation (1) of the main manuscript with an absolute value. These results show that our quantum holographic

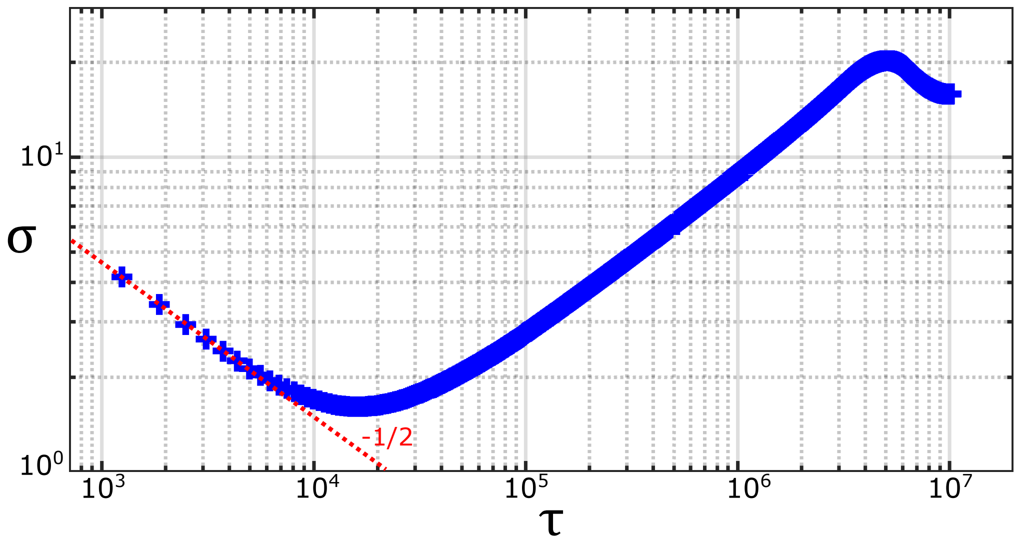

*Figure L: **Allan deviation plot**. Allan deviation values σ (blue crosses) are represented in function of the averaging time τ, together with a $-1/2$ slope (red). Time unit is in number of frames.*

approach can be used as a practical tool for phase and amplitude measurements of complex objects, including biological samples.

Figure N shows photos of the microscope slides containing the bird feather and the piece of scotch tape.

Our quantum holographic scheme is currently limited to image the phase of polarisation-sensitive objects. To extend its range of application, Figure O.a shows a modified version of our experimental setup that can be used to achieve quantum holography with non-polarisation sensitive object. This configuration harnesses concepts from Differential Interference Contrast microscopy [27]. In this new configuration, Alice SLM is not used anymore (i.e. flat phase mask shown in Figure O.b) and is replaced by a non-birefringent sample located in a conjugated image

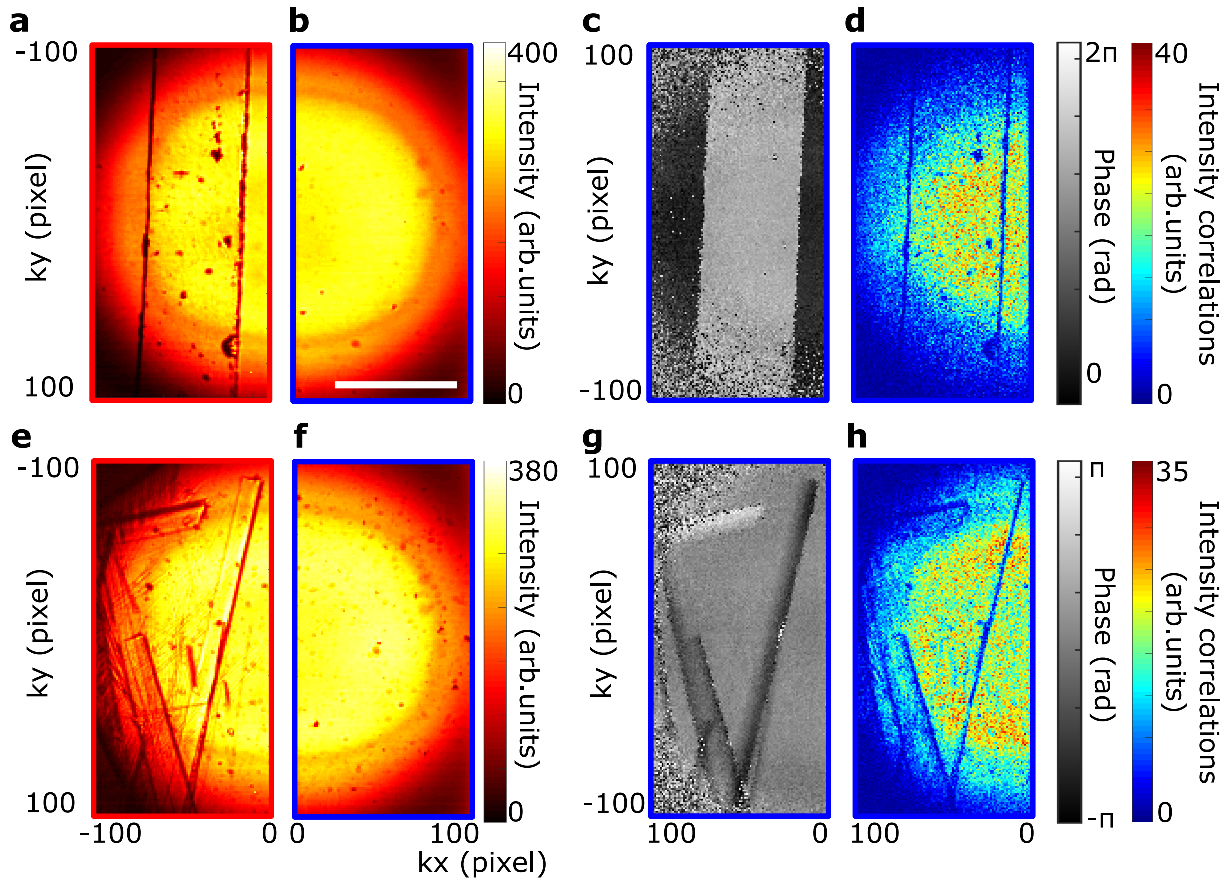

Figure M: ***Quantum holographic imaging of real objects. a****, Intensity images measured by Alice showing a piece of transparent scotch tape.* ***b****, Intensity image measured by Bob.* ***c****, Phase image reconstructed by Bob with SNR=* 14*.* ***d****, Amplitude image reconstructed by Bob from the same set of intensity correlation images by replacing the argument in equation (1) of the manuscript with an absolute value.* ***e****, Intensity image measured by Alice showing parts of a bird feather.* ***f****, Intensity image measured by Bob.* ***g****, Phase image reconstructed by Bob with SNR=* 13*.* ***h****, Amplitude image reconstructed by Bob.* 10^7 *frames were acquired in total for each case. The white scale bar corresponds to* 1*mm. Phase and amplitude images retrieved by Bob are rotated by 180 degrees for convenience.*

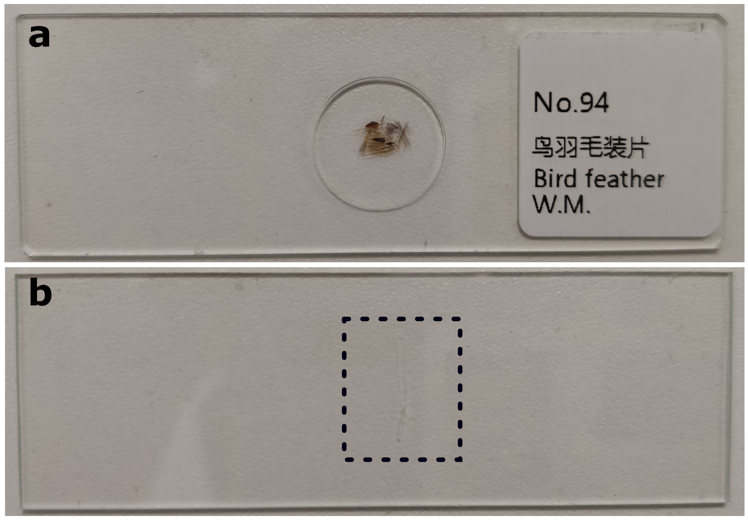

Figure N: ***Photos of microscope slides****.* ***a****, Bird feather on a microscope slide provided by the company KKmoon.* ***b****, Piece of scotch tape on a microscope slide from the company Sellotape.*

plane positioned between lenses f_3 and f_4. Furthermore, two Savart plates are positioned just before and after the sample: the first plate separates the incident beam into two parallel beams and the second plate recombine them. In our experiments, the Savart plates are made of two layers of quartz of 3 mm thickness, with optical axes tilted at 45 degrees with respect to the surface normal. Each SP produces a shear of approximately 25 µm. As detailed in [28], such arrangement produces a polarisation-sensitive phase pattern at its output that is directly proportional to the spatial phase of the non-birefringent sample inserted between the plates. Figures O.c-h show preliminary results of phase measurement of a random phase layer fabricated by spraying some silicone adhesive onto a microscopic slide. When using our conventional experimental (without the Savart plates), we clearly observe that the sample is not polarisation dependent because no phase variation are visible in the reconstructed phase in Figure O.e. In contrary, the phase measured using the new experimental configuration in Figure O.g shows random spatial variations of the phase, confirming that our quantum holographic scheme is now sensitive to non-polarisation sensitive objects.

11 Phase imaging through static phase disorder

Figure O.e shows a phase image reconstructed using the conventional quantum imaging setup (i.e. setup in Figure O.a without the Savart plates) of a flat phase object programmed on Alice SLM (Figure O.b) in the presence of a static random non-birefringent phase disorder on the optical path. The absence of any phase variations in Figure O.e shows that our holographic protocol is also insensitive to the presence of static phase disorder, thus confirming that the dynamics of the disorder has no influence (e.g. as an averaging effect) on the robustness of the phase disorder advantage demonstrated in Figure 3 in the manuscript.

12 Details on decoherence free subspace and collective dephasing

By definition, a decoherence free subspace (DFS) is a subspace of the Hilbert space of a quantum system that is invariant to non-unitary dynamics e.g. dynamic dephasing. In our experiment, the subspace spanned by the states $|HH\rangle$ and $|VV\rangle$ is invariant to a dynamic dephasing process, that is a non-unitary evolution operator, and is then by definition a DFS [29].

The notion of DFS is strongly linked to the properties of the decoherence effect. The decoherence effect considered in our work is a type of *collective* dephasing process. A general dephasing process corresponds to a qubit state $|P\rangle_k$ (where P and k are the polarisation and spatial mode of a photon, respectively) that undergoes a random phase shift $\phi_{P,k}$ varying over time:

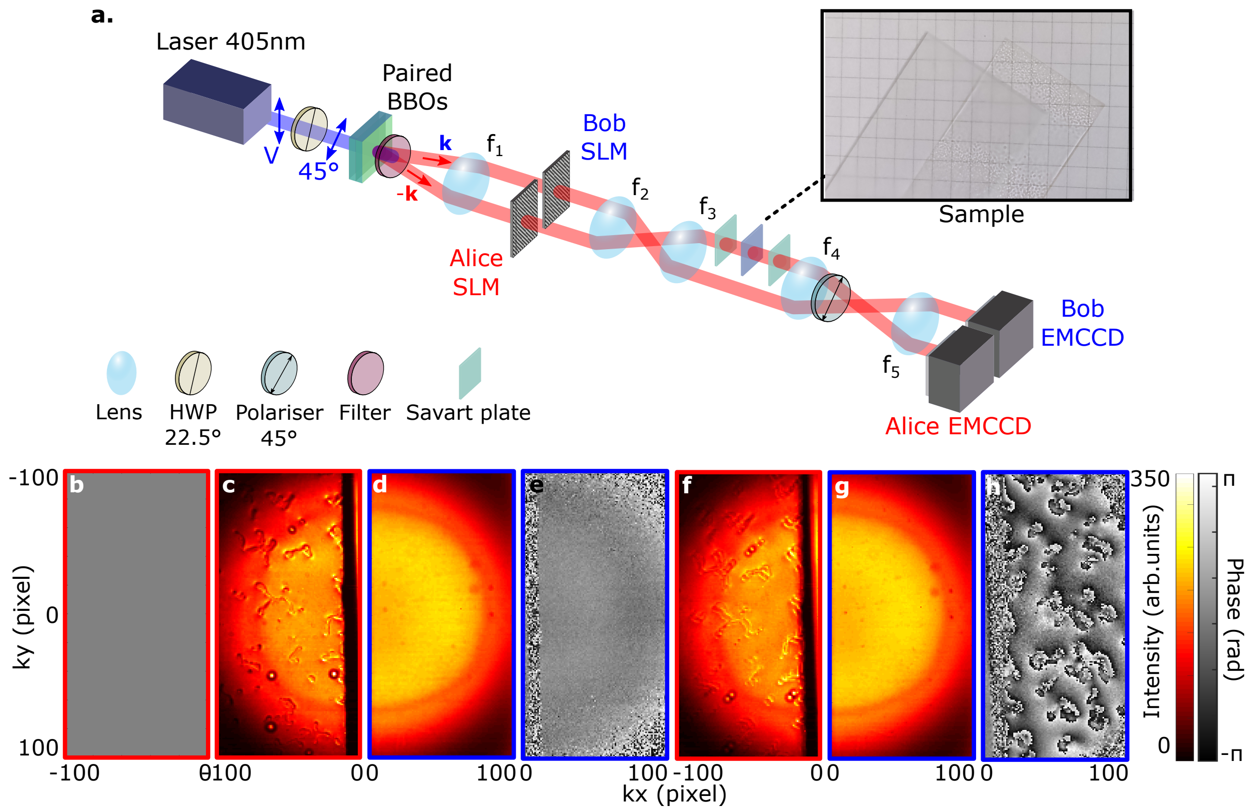

Figure O: ***Quantum holography of non-polarisation sensitive objects***. ***a***, *Modified quantum holographic setup to achieve phase imaging of non-polarisation sensitive phase object. The sample is inserted in a conjugate image plane of Alice SLM located between* f_3 *and* f_4*. Two Savart plates are inserted on each side of the sample and are slightly tilted. The sample is a microscopic slide covered by a layer of silicone adhesive generated using a spay, that effectively produces a random phase layer.* ***b***, *Flat phase pattern on Alice SLM (not in use in this configuration),* ***c*** *and* ***d***, *Intensity images measured by Alice and Bob without the Savart plates.* ***e***, *Phase reconstructed by Bob using the quantum holographic approach without the Savart plates with SNR=* 17. ***f*** *and* ***g***, *Intensity images measured by Alice and Bob with the Savart plates.* ***h***, *Phase reconstructed by Bob using the quantum holographic approach with the Savart plates with SNR=* 12*. Each phase image was reconstructed from* 5.10^6 *frames.*

$|P\rangle_k \rightarrow e^{i\phi_{P,k}}|P\rangle_k$. Such process is called *collective* if they are some correlations between the random phases applied to the different qubits that persist over time. For example, in many previous works on DFS [30,31], these correlations are spatial: two different qubits $\{|P_1\rangle_{k_1}, |P_2\rangle_{k_2}\}$ undergo random phase shifts ϕ_{P_1,k_1} and ϕ_{P_2,k_2} that vary over time but remain correlated in space at any time i.e. $\phi_{P,k_1} = \phi_{P,k_2}$, where P denotes indifferently P_1 or P_2. While this form of decoherence is relevant in quantum information processing and communication applications, it is less realistic in our imaging configuration. In our case, the presence of two non-correlated non-birefringent dynamic random phase disorder on two different optical paths produces another form of collective decoherence in which the random phases are not correlated in space but in polarisation i.e. $\phi_{P_1,k} = \phi_{P_2,k}$, where k can be indifferently k_1 or k_2.

13 Details on imaging in the presence of classical stray light using quantum illumination (QI)

The QI protocol was introduced by S.Lloyd [32] and extended to Gaussian states by Tan et al [33], in which a practical version of the protocol is proposed. In imaging, the protocol has been suggested for detecting the presence of an object embedded within a noisy background, even in the presence of environmental perturbations and losses [34,35]. In 2013, Lopaeva et al. [36] performed the first experimental demonstration of the QI protocol to determine the presence an object by exploiting intensity correlations between photons produced by parametric down conversion. Very recently, spatial correlations between downconverted photon pairs have been used to implement full-field QI protocols [18,37], where amplitude objects were reconstructed through coincidence measurements performed by a camera in the presence of static stray light. In our work, the QI protocol is based on similar arrangements than those used in [37] i.e. one photon of an entangled pair illuminates an object while the other is used as an 'ancilla', and both photons are detected in coincidence using a camera in the presence of classical light. However, our QI protocol goes beyond these previous works because it operates for phase objects (that are completely invisible on the intensity images, as shown for example in Figure I where only the cat-shaped objects are visible) and also works in the presence of dynamic stray light i.e. a time-varying complex speckle pattern superimposed on the sensor. Note also that another difference is that our experiment employs a source of photon pairs entangled not only in space but also polarisation, in which the spatial entanglement is certainly at the base of the QI advantage, but where polarisation entanglement is still required for the holographic process.

1. Defienne, H., Reichert, M. & Fleischer, J. W. General model of photon-pair detection with an image sensor. *Physical review letters* **120**, 203604 (2018).

2. Barreiro, J. T., Langford, N. K., Peters, N. A. & Kwiat, P. G. Generation of Hyperentangled Photon Pairs. *Physical Review Letters* **95**, 260501 (2005).

3. Howell, J. C., Bennink, R. S., Bentley, S. J. & Boyd, R. W. Realization of the Einstein-Podolsky-Rosen Paradox Using Momentum- and Position-Entangled Photons from Spontaneous Parametric Down Conversion. *Physical Review Letters* **92**, 210403 (2004).

4. Moreau, P.-A., Mougin-Sisini, J., Devaux, F. & Lantz, E. Realization of the purely spatial Einstein-Podolsky-Rosen paradox in full-field images of spontaneous parametric down-conversion. *Physical Review A* **86**, 010101 (2012).

5. Tasca, D. S. *et al.* Imaging high-dimensional spatial entanglement with a camera. *Nature Communications* **3**, 984 (2012).

6. Fedorov, M. V., Mikhailova, Y. M. & Volkov, P. A. Gaussian modelling and Schmidt modes of SPDC biphoton states. *Journal of Physics B: Atomic, Molecular and Optical Physics* **42**, 175503 (2009).

7. Chan, K. W., Torres, J. P. & Eberly, J. H. Transverse entanglement migration in Hilbert space. *Physical Review A* **75**, 050101 (2007).

8. Schneeloch, J. & Howell, J. C. Introduction to the transverse spatial correlations in spontaneous parametric down-conversion through the biphoton birth zone. *Journal of Optics* **18**, 053501 (2016).

9. Clauser, J. F., Horne, M. A., Shimony, A. & Holt, R. A. Proposed Experiment to Test Local Hidden-Variable Theories. *Physical Review Letters* **23**, 880–884 (1969).

10. Aspect, A., Grangier, P. & Roger, G. Experimental realization of Einstein-Podolsky-Rosen-Bohm Gedankenexperiment: a new violation of Bell's inequalities. *Physical review letters* **49**, 91 (1982).

11. Hegazy, S. F. & Obayya, S. S. A. Tunable spatial–spectral phase compensation of type-I (ooe) hyperentangled photons. *JOSA B* **32**, 445–450 (2015).

12. Hegazy, S. F., Badr, Y. A. & Obayya, S. S. A. Relative-phase and time-delay maps all over the emission cone of hyperentangled photon source. *Optical Engineering* **56**, 026114 (2017).

13. Jha, A. K. & Boyd, R. W. Spatial two-photon coherence of the entangled field produced by down-conversion using a partially spatially coherent pump beam. *Physical Review A* **81**, 013828 (2010).

14. Kulkarni, G., Subrahmanyam, V. & Jha, A. K. Intrinsic upper bound on two-qubit polarization entanglement predetermined by pump polarization correlations in parametric down-conversion. *Physical Review A* **93**, 063842 (2016).

15. Kulkarni, G., Kumar, P. & Jha, A. K. Transfer of temporal coherence in parametric down-conversion. *JOSA B* **34**, 1637–1643 (2017).

16. Fienup, J. R. Phase retrieval algorithms: a comparison. *Applied Optics* **21**, 2758 (1982).

17. Yamaguchi, I. & Zhang, T. Phase-shifting digital holography. *Optics Letters* **22**, 1268–1270 (1997).

18. Defienne, H., Reichert, M., Fleischer, J. W. & Faccio, D. Quantum image distillation. *Science Advances* **5**, eaax0307 (2019).

19. Reichert, M., Defienne, H. & Fleischer, J. W. Optimizing the signal-to-noise ratio of biphoton distribution measurements. *Physical Review A* **98**, 013841 (2018).

20. Goodman, J. W. *Introduction to Fourier Optics* (Roberts and Company Publishers, 2005). Google-Books-ID: ow5xs_Rtt9AC.

21. Defienne, H., Reichert, M. & Fleischer, J. W. Adaptive Quantum Optics with Spatially Entangled Photon Pairs. *Physical Review Letters* **121**, 233601 (2018).

22. Devaux, F., Mosset, A., Bassignot, F. & Lantz, E. Quantum holography with biphotons of high Schmidt number. *Physical Review A* **99**, 033854 (2019).

23. Boto, A. N. *et al.* Quantum Interferometric Optical Lithography: Exploiting Entanglement to Beat the Diffraction Limit. *Physical Review Letters* **85**, 2733–2736 (2000).

24. Abouraddy, A. F., Saleh, B. E., Sergienko, A. V. & Teich, M. C. Entangled-photon Fourier optics. *JOSA B* **19**, 1174–1184 (2002).

25. Allan, D. W. Statistics of atomic frequency standards. *Proceedings of the IEEE* **54**, 221–230 (1966). Publisher: IEEE.

26. Variance, A. Noise Analysis for Gyroscopes. *Freescale Semiconductor Document Number: AN5087 Application Note Rev. 0* **2** (2015).

27. Allen, R. D. & David, G. B. The Zeiss-Nomarski differential interference equipment for transmitted-light microscopy. *Zeitschrift fur wissenschaftliche Mikroskopie und mikroskopische Technik* **69**, 193–221 (1969).

28. Terborg, R. A., Pello, J., Mannelli, I., Torres, J. P. & Pruneri, V. Ultrasensitive interferometric on-chip microscopy of transparent objects. *Science Advances* **2**, e1600077 (2016).

29. Lidar, D. A. & Birgitta Whaley, K. Decoherence-Free Subspaces and Subsystems. In Benatti, F. & Floreanini, R. (eds.) *Irreversible Quantum Dynamics*, Lecture Notes in Physics, 83–120 (Springer, Berlin, Heidelberg, 2003).

30. Kwiat, P. G., Barraza-Lopez, S., Stefanov, A. & Gisin, N. Experimental entanglement distillation and 'hidden' non-locality. *Nature* **409**, 1014–1017 (2001).

31. Banaszek, K., Dragan, A., Wasilewski, W. & Radzewicz, C. Experimental Demonstration of Entanglement-Enhanced Classical Communication over a Quantum Channel with Correlated Noise. *Physical Review Letters* **92**, 257901 (2004).

32. Lloyd, S. Enhanced Sensitivity of Photodetection via Quantum Illumination. *Science* **321**, 1463–1465 (2008).

33. Tan, S.-H. *et al.* Quantum Illumination with Gaussian States. *Physical Review Letters* **101**, 253601 (2008).

34. Guha, S. & Erkmen, B. I. Gaussian-state quantum-illumination receivers for target detection. *Physical Review A* **80**, 052310 (2009).

35. Pirandola, S., Bardhan, B. R., Gehring, T., Weedbrook, C. & Lloyd, S. Advances in photonic quantum sensing. *Nature Photonics* **12**, 724–733 (2018).

36. Lopaeva, E. D. *et al.* Experimental Realization of Quantum Illumination. *Physical Review Letters* **110**, 153603 (2013).

37. Gregory, T., Moreau, P.-A., Toninelli, E. & Padgett, M. J. Imaging through noise with quantum illumination. *Science Advances* **6**, eaay2652 (2020).